applied optics

Low-cost fabrication of microlasers based on polymeric micropedestals

H. M. Reynoso-de la Cruz,[1] ● E. Ortiz-Ricardo,[2] ● V. A. Camarena-Chávez,[1] ●
A. Martínez-Borquez,[3] ● G. Gutiérrez-Juárez,[1,4] ● A. B. U'Ren,[2,5] ● AND
R. Castro-Beltrán[1,4,*] ●

[1]*División de Ciencias e Ingenierías de la Universidad de Guanajuato, Departamento de Ingeniería física, Cuerpo Académico de Mecánica Estadística, León, Gto., Mexico*
[2]*Instituto de Ciencias Nucleares, Universidad Nacional Autónoma de México, apdo. postal 70-543, 04510 D.F., Mexico*
[3]*Escuela de Ingeniería y Ciencias, Tecnológico de Monterrey Campus León, Edificio CCI, 2nd piso, León, Guanajuato, Mexico*
[4]*Cuerpo Académico de Mecánica Estadística, Departamento de Ingeniería Física, Guanajuato, Mexico*
[5]*e-mail: alfred.uren@correo.nucleares.unam.mx*
Corresponding author: cbrigoberto@fisica.ugto.mx

Our current work exploits direct laser writing (DLW) and low one-photon absorption (LOPA) in a low-cost three-dimensional optical fabrication system designed to print micrometric polymeric structures. Micropedestals were obtained by focusing a laser beam on a photoresist layer deposited on a silica glass substrate. Subsequent coating with rhodamine 6G dye allows these pedestals to function as microlasers upon optical excitation at 532 nm. Our microlasers, with a diameter of ∼53 µm and a height of ∼40 µm, exhibit a broad fluorescence peak in the spectral range 540–600 nm, in addition to narrow lasing peaks, exhibiting quality factors Q exceeding 2000 and a lasing threshold of ∼5 µJcm^{-2}. The observed free spectral range associated with the lasing peaks of ∼1.3 nm is consistent with simulations, which we include in this paper. In addition, we present simulations for the longitudinal shift of the patterning laser spot, which occurs particularly for relatively thick photoresist layers, coupled with a large index contrast at the photoresist top surface. Such a shift could introduce errors in the resulting microfabricated structures if left unaccounted for. We hope that our work will contribute to the development of microlasers for various photonic applications, particularly if dimensions can be reduced, for on-chip optical communications and data processing. © 2021 Optical Society of America

https://doi.org/10.1364/AO.410615

1. INTRODUCTION

In order to fabricate micrometric-scale polymeric structures, technologies such as standard photolithography [1], holography [2], stereolithography [3], "inkjet" printing [4,5], and direct laser writing (DLW) [6–8] have been used. Some of these methods are well suited for parallel manufacturing and hold the potential to optically address submicrometer structures. While inkjet printing has been shown to constitute a robust technique for the fabrication of microlaser arrays with competitively large Q factors and low lasing thresholds, DLW leads to the possibility of fabricating 2D and 3D structures enabled by the full freedom of motion in the xyz axes during fabrication, limited only by the mechanical resolution and the laser spot size [6,7]. For example, Do *et al.* used DLW in order to print spiral, chiral, and woodpile structures, with potential implications on controlling the directionality of laser emission, and on integrated nanophotonics through interconnected blocks [6,9].

In a DLW implementation, a photoresist sample is exposed to optical radiation, so that the laser beam and the photoresist can interact through one-photon absorption (OPA), two-photon absorption (TPA), and/or low one-photon absorption (LOPA); these processes govern the laser writing process [7,8,10]. TPA, a nonlinear optical absorption phenomenon, is mainly associated with the use of a pulsed laser, e.g., a fs Ti:sapphire oscillator [10]. In contrast, OPA and LOPA are linear optical processes that can be implemented with a continuous-wave laser of low optical power, typically in the near UV and visible regions, respectively.

When comparing the OPA and the LOPA mechanisms, the OPA process is associated with conventional photolithography, which permits fabrication of 1D and 2D microstructures [11]. On the other hand, the LOPA mechanism combines the best features of OPA and TPA. For example, LOPA implies a very low optical absorption condition inside the photoresist, which opens the possibility of deeper penetration of the laser

beam into the photosensible material. Moreover, since the photopolymerization will occur preferentially in areas of maximum optical intensity, the resulting microstructures can resemble state-of-the-art TPA results [6,10,12].

The fabrication of micropedestals has been demonstrated with a wide range of dimensions, ranging in diameter from a few to several hundred micrometers (μm). While pedestals at the low end of this range are naturally suited for integrated optics applications, larger structures such as the ones we obtain (see below) have a number of possible applications. Particularly, such pedestals could be used for biomedical applications, including for example for *in situ* microindentation tests on bone tissue [13], as microneedle holders for transdermal drug delivery [14], and in the study of subtle force patterns in microorganisms (for example in *Caenorhabditis elegans*) [15]. In the field of microfluidics, such micropillars have been used for controllable microfluidic mixing [16,17]. Likewise, in the area of photonics a natural application is for laser microcavities [18,19], which we concentrate on in this paper.

The present work aims to demonstrate the potential of DLW based on LOPA as the basis for high-quality solid micropedestal fabrication, particularly to be used as microlasers [20–23]. We have aimed to keep the costs of our microfabrication apparatus as low as possible, with the use of a simple laser rather than a direct-write station with vibration control. Our full fabrication system (a previous version of which was presented in Ref. [8]) including the DLW laser, the computer-controlled xyz translation stage, and other optical/optomechanic components, has a combined cost around US\$1000 (excluding the postfabrication microlaser characterization apparatus). We note that all software used in our system is free and nonproprietary, with the implication that it can be modified as needed by the user. A system like ours can be set up and later modified as needed by the end user, possibly by advanced undergraduate students, without the need for external technicians.

In this work we also present simulations for the longitudinal shift of the patterning laser spot, which occurs particularly for relatively thick photoresist layers, coupled with a large index of refraction contrast at the photoresist top surface, as in our fabrication conditions. Note that such a shift (which would become negligible in our experimental setup for photoresist layers with $\lesssim 15$ μm thicknesses or for larger thicknesses if an oil-immersion objective is used for focusing the pattering beam), could introduce errors in the resulting microfabricated structures if left unaccounted for.

The design and application of our organic microlasers, based on a hybrid conception of i) micropedestal fabrication and ii) coating with laser dyes, facilitates the application routes towards low-power-consumption devices including full-color microlaser arrays and micrometric-scale objects that can interact with biological tissue via spontaneous processes for super-resolution imaging, among others [5,20,24,25]. Provided device dimensions can be reduced, our fabrication protocol could in the future also be used for integrated optics applications. We believe that our simple yet versatile and low-cost platform could constitute a competitive alternative for micrometric-scale optical fabrication and its derived applications, particularly for microlaser devices.

2. LASER DIRECT-WRITE SYSTEM AND THE FABRICATION PROTOCOL

The schematic representation of our laser direct-write platform is presented in Fig. 1(a), which includes a CW laser operating at 532 nm (Civil Laser-LSR532NL-300) and a 5× microscope objective (MO) with a numerical aperture (NA) of 0.13 (Motic achromatic objective) that focuses the laser beam on the sample.

The trajectory of the optical beam prior to the MO is controlled by a set of broadband dielectric mirrors. The sample to be patterned is placed on a holder attached directly to a computer-controlled xyz translation stage. Note that throughout this work the $x-y$ plane is parallel to the top surface of the sample, while the z axis corresponds to the propagation depth in the sample. The mechanical resolution of the stage is 2 μm, while the optical resolution was determined experimentally to be along z (governed by the beam's Rayleigh range) ~40 μm and transversely on the $x-y$ plane ~4 μm.

The intensity pattern at the sample depends strongly on the quality of the laser's spatial emission mode as well as on the properties of the MO. The electric field intensity in the focal region determines the dimensions and morphology of the printed patterns, and it can be modeled through the vectorial Debye–Wolf diffraction integral [26,27] in Eq. (1):
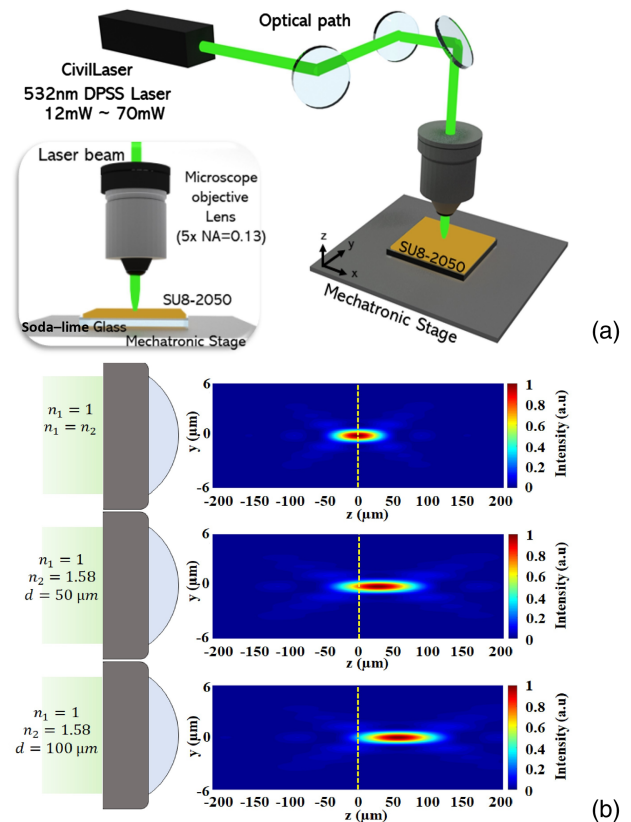

Fig. 1. (a) Experimental setup used for the optical fabrication device. The beam from a low-cost laser at 532 nm is focused on the sample using a 5× microscope objective with a numerical aperture of 0.13. (b) Simulations of the intensity distributions along the $y-z$ plane for three cases: i) no interface, ii) an interface with $d = 50$ μm thickness, and iii) with $d = 100$ μm thickness.

$$\mathbf{E}(x_2, y_2, z_2) = -\frac{iC}{\lambda} \int_0^\alpha d\phi \int_0^{2\pi} d\theta_1 \sin\theta_1 \sqrt{\cos\theta_1} A(\theta_1, \phi)$$

$$\times \mathbf{P_2}(\theta_1, \phi) \exp[ik((n_2 z_2 \cos\theta_2$$

$$+ n_1 x_2 \sin\theta_1 \cos\phi + n_1 y_2 \sin\theta_1 \sin\phi)$$

$$+ \Phi(\theta_1, \theta_2, \phi))].$$

$$\tag{1}$$

In Eq. (1) we have assumed an interface between two distinct media, in our specific case, air (subscript 1) and the SU8-photoresist layer (subscript 2) with refractive indices n_1 and n_2, through which the beam propagates. θ_1 represents a polar angle subtended with the z axis, while ϕ is an azimuthal angle on the $x-y$ plane. θ_2 accounts for refraction at the interface, i.e., $n_1 \sin(\theta_1) = n_2 \sin(\theta_2)$. $A(\theta_1, \phi)$ represents the incident transverse electric field distribution, $\mathbf{P_2}(\theta_1, \phi)$ represents the incident polarization distribution [8,26,27], C is a constant proportional to the laser power, and $\alpha = \arcsin(NA/n)$. For the numerical calculations presented below, we assume a uniform beam, i.e., $A(\theta_1, \phi) = 1$, within the integration region defined by the numerical aperture. The function Φ, describing the induced aberration, is dependent on the distance between the dielectric interface and the focal plane, and it can be expressed as $\Phi(\theta_1, \theta_2, \phi) = -d(n_1 \cos\theta_1 - n_2 \cos\theta_2)$, where we assume that patterning occurs at a depth in the second material (in our case SU8) close to its thickness d. Figure 1(b) presents numerical calculations, based on Eq. (1), of the electric field intensity distribution $|\mathbf{E}(x_2, y_2, z_2)|^2$ along the $x-z$ plane for a MO with NA of 0.13. From top to bottom, Fig. 1(b) shows the behavior of the spatial intensity distribution in the focal region for three cases: i) only air (i.e., no interface, with $n_1 = n_2 = 1$), ii) $d = 50$ μm, and iii) $d = 100$ μm. It becomes evident that there is a longitudinal shift of the beam waist, away from the interface and into the photoresist, which is dependent on the thickness d; in general, this shift will become noticeable for relatively thick photoresist layer (under our experimental conditions $d \gtrsim 15$ μm), in addition to a relatively large index contrast at the top photoresist surface (as in our experiment involving an air–SU8 interface). This effect, caused by the induced aberration, should be taken into consideration in the experimental procedure, as it can be a source of imperfections in the resulting morphology of the fabricated objects. For example, the induced shift for an interface with $d = 100$ μm is ~60 μm, i.e., of the same order of magnitude as the longitudinal dimensions of the intended resulting fabricated objects.

While from the above simulations the full width at half-maximum spot diameter is ~2.9 μm, in practice, various experimental imperfections result in a larger optical spot. The parameters used to simulate the electric field intensity distribution were $\lambda = 532$ nm, $n_1 = 1.00$, and $n_2 = 1.58$.

For the present work we have built an optical fabrication platform, described above, relying on laser direct writing with computer-controlled xyz patterning [8]. Our system allows the user to define various parameters such as the specific xyz motion trajectory to be executed, the number of repetitions of this trajectory, as well as the speed at which this motion occurs. In the specific case of the results presented here, involving micropedestals, the laser beam is left stationary, i.e., the

trajectory is composed of a single point. Through a systematic exploration of the exposure time, optical power level, and position along z of the focal region, we have determined combinations of parameters that yield the best quality in the resulting microstructures.

SU8-2050 photoresist (a negative photoresist material, part of the SU8-2000 series; MicroChem-Negative Photoresist) is used for the fabrication of the micropedestals. The film deposition on a conventional glass substrate (in our case, soda–lime glass; SLG) is achieved through spin coating. Note that because our micropedestals are designed to operate as whispering-gallery oscillators (with the oscillation plane parallel to the substrate surface), the confined optical radiation essentially does not interact with the substrate, so additional substrate preparation (e.g., application of a Bragg reflector) is unwarranted [4,5].

Briefly, a ~2 ml drop of photoresist is deposited onto the SLG substrate and a film thickness of ~100 μm is obtained through spin coating. Once the spin coating has been completed, the sample is soft-baked at 45°C for 4 min to remove any residual SU8 solvent. After exposing the sample to laser radiation for printing the desired pattern, it is post-exposed to the final baking treatment (post-exposure bake (PEB) at 45°C for 7 min. PEB treatment is followed by the development process in which the sample is placed in a SU8-2050 developing bath to obtain the final structures.

In the following section we present, on the one hand, the samples obtained through the fabrication protocol described above, and on the other hand, we describe the successful application of these samples as microlasers.

3. ORGANIC PEDESTAL MICROLASERS

In this work, we demonstrate the low-cost and repeatable DLW fabrication of micrometric structures (in particular, solid cylindrical polymeric pedestal microcavities), which can be coated with rhodamine 6G dye (R6G) so as to permit lasing.

We have fabricated different sets of micropedestals using a $5\times$ MO with $NA = 0.13$ and 50 mW laser power. Following the fabrication process, each sample was coated with 10^{-4} M of R6G dissolved in methanol; a 4 μL drop of the solution is deposited on the micropedestal with the help of a microliter (μL) pipette. Figure 2 shows an example of one of our resulting high-quality coated micropedestals, obtained with a 5 min exposure time. Our printed micropedestals show a diameter and height of 53 ± 1 μm and 40 ± 1 μm, respectively. The fact that our resulting structures are considerably larger than the spot size used during fabrication is probably the result of scattering of the patterning beam due to irregularities, including index of refraction variations produced through thermal effects, which may appear during the photopolymerization process [7,28].

Figure 2(a) shows the reproducibility in the manufacturing process of the pedestals under the use of the platform and the DLW photolithographic protocol. The photograph of the micropedestal in Fig. 2(b), under optical excitation, exhibits a yellowish hue, which is attributed to fluorescence and lasing spectral peaks circulating in the cavity, some of which escape due to scattering from imperfections (e.g., including surface roughness) [22,29–31]. Panels (c) and (d) show an uncoated and a coated micropedestal, respectively.
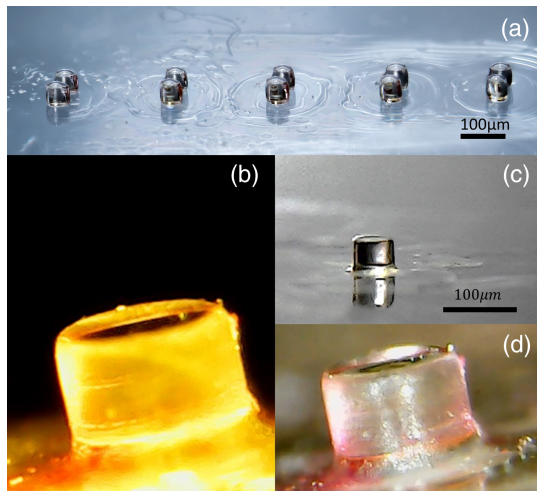
Fig. 2. (a) Set of reproducible micropedestals. (b) Fluorescence microscopy image of the optically excited micropedestal (with ~53 μm diameter and ~40 μm height), coated with rhodamine 6G. (c) and (d) Close-ups of the uncoated and coated devices, respectively.
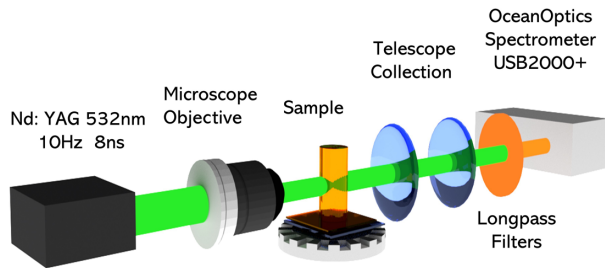

Fig. 3. Experimental setup for the characterization of the hybrid micropedestals. A microscope objective with a numerical aperture NA = 0.13 focuses the laser beam, which impinges tangentially on the sample's cylindrical sidewall.

From Fig. 2, it may be appreciated that the micropedestal presents a well-defined cylindrical shape with a circular transverse section (i.e., along the $x-y$ plane). In order to characterize optically the microcavities, we carried out measurements of the emission spectra using the experimental setup shown in Fig. 3. A pulsed laser at 532 nm with a repetition rate of 10 Hz and a pulse duration of 8 ns (Quantel Brilliant B 360 MJ) is focused on the sample (with a NA = 0.13 microscope objective) and thus optically excites the microcavity with a pump fluence ranging from 2 μJcm^{-2} to 12 μJcm^{-2}. The residual pump power is suppressed with two long-pass filters placed in series. The cavity rests on a mechanical platform, which permits translation along the xyz axes as well as rotation on the $x-y$ plane. The optical radiation from the cavity, transmitted by the long-pass filters, is conveyed with a telescope to the input port of a USB spectrometer (Ocean optics USB2000-UV-vis with 200–850 nm detection range). Once the best experimental conditions in terms of excitation, detection, sample position, and signal-to-noise ratio were established, the emission spectra data is acquired through a set of 10 measurements, each one with a 500 ms integration time.

An example of an emission spectrum obtained through the set of steps described in the previous paragraph is shown
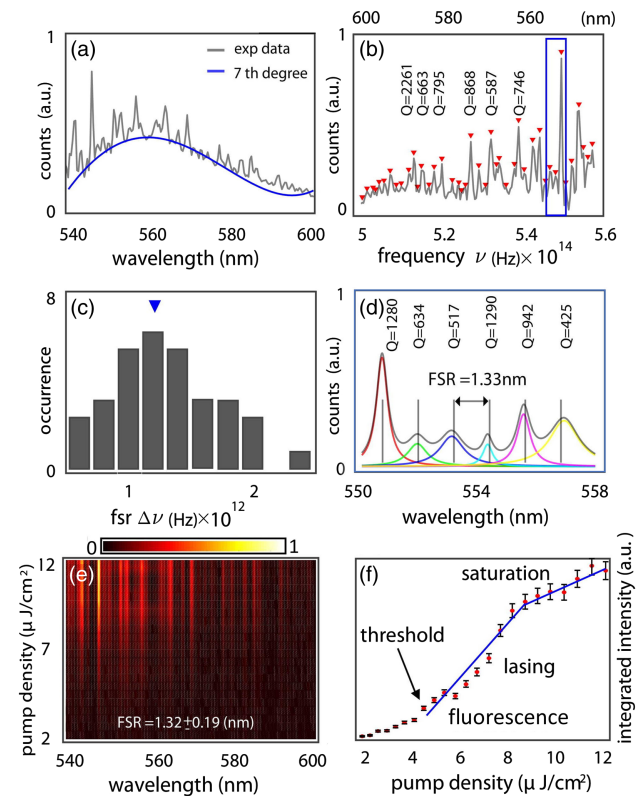

Fig. 4. Spectrum from a micropedestal with a diameter of ~53 μm and height 40 μm; (a) raw spectrum obtained at a fluence of 12 μJcm^{-2} together with fit (using seventh-degree polynomial) to the broad fluorescence background and (b) the lasing peaks obtained by subtracting the broad-peak fit from the raw spectrum. (c) Histogram of neighboring peak spectral separations, yielding the FSR. (d) Close-up of one of the laser emission regions, within the blue rectangle of panel (c), fitted to Lorentzian peaks with the corresponding Q factors. (e) Narrow lasing peaks as a function of wavelength (horizontal axis) and pump fluence (vertical axis). (f) λ-integrated total collected flux as a function of the pump fluence.

in Fig. 4(a). A visual inspection of this spectrum shows the presence of a sequence of narrow spectral peaks with a broad underlying fluorescence peak. So as to isolate the narrow peaks, which we associate with lasing action, we first characterize the broad peak. For this purpose we perform a fit of the data set, from which points within the narrow peaks are excluded, to a seventh-order polynomial, which is plotted along with the full emission spectrum in Fig. 4(a). The subtraction of this fitted background peak from the full emission data, as plotted in Fig. 4(b), yields the sequence of narrow spectral peaks (each peak indicated with a red triangle). From this sequence of spectral peaks, we now compute the spectral separation between each pair of neighboring peaks and plot a histogram of spectral separations as shown in Fig. 4(c) (plotted as a function of frequency so as to avoid the inherent λ^2 dependence of the expression for the FSR when written in terms of wavelength [32]). By fitting a Gaussian function to this histogram we estimate the FSR of our laser microcavity to be FSR = 1.32 ± 0.19 nm.

In order to further analyze the resulting lasing spectral peaks, we have fitted Lorentzian curves to individual peaks, within the spectral window indicated with a blue rectangle in Fig. 4(b).

We have plotted both the individual Lorentzian fits as well as their sum in Fig. 4(d). From these fits, we compute the Q factor for each peak as the quotient of the central peak frequency to the full width at half-maximum spectral width. We have indicated the Q values thus obtained in Fig. 4(d), with values ranging from the hundreds to the thousands. The resulting Q values agree well with those reported in the literature for polymeric microlasers [22,23,33–36]. These relatively low Q values are probably related to scattering due to sidewall roughness and other imperfections in our micropedestals [22,31].

In Fig. 4 we present the behavior of the fluorescence and lasing peaks upon optical excitation of our dye-coated micropedestals. In Fig. 4(e), we plot the experimental emission spectra (with wavelength in the horizontal axis) as a function of the pump fluence (in the vertical axis). This plot makes it clear that the spectral position and shape of each of the lasing peaks remain unaffected by varying the pump fluence. In order to clarify that the emission characteristics are consistent with lasing action, we have plotted in Fig. 4(f) the total flux versus pump fluence, i.e., integrated over wavelength. At pump fluences below $\sim 5 \ \mu \text{Jcm}^{-2}$, the behavior of the emission spectra can be associated with simple spontaneous emission, while, at pump fluences above this value, the behavior changes abruptly with a slope enhancement by a factor of ~ 3.3 with respect to the spontaneous emission observed at lower fluences, indicating the onset of lasing. For fluences above $\sim 9 \ \mu \text{Jcm}^{-2}$ the slope decreases, indicating a saturation phenomenon [5,18,22,30,37]. Note that the inferred lasing threshold of around $\sim 5 \ \mu \text{Jcm}^{-2}$ is consistent with those reported in the literature for devices with similar shape, dimensions, and Q factors [23,33–35,38].

For cylindrical resonators, it is known that light can be confined: i) as a Fabry–Perot (FP) mode for which light oscillates between the two opposite flat ends of the cylinder and ii) as a whispering-gallery (WG) mode for which the light circulates around the cylinder's perimeter [19,39]. In our case, considering that the micropedestals are mounted with the cylinder's axis normal to the laser beam propagation direction, excitation occurs tangentially to the circular cylinder cross section, and it is therefore WG modes that can be excited [30,36,38].

We note that in our experiments, based on WG oscillation, light can escape the cavity at any cavity azimuthal location due to scattering from surface roughness and/or imperfections. This implies that while the laser radiation (as well as the fluorescence) produced can be emitted in all directions within the oscillation plane, only a fraction (corresponding to the acceptance solid angle of the detection apparatus) can be collected. This tends to limit the signal-to-noise ratio in our measurements. We note that a future improvement to our work will involve evanescent coupling of the micropedestals to an external waveguide for a more controlled and directional collection of the laser radiation. In addition, better control of fabrication conditions (so as to restrict surface imperfections) could lead to increased Q values and reduced lasing thresholds. The relatively large range of Q values obtained in our experiment is linked to the low signal-to-noise ratio discussed above, which affects peaks with a lower height to a greater degree. In addition, we note that our fluorescence/laser peak spectrum measurements are near the resolution limit of our spectrometer (with three or fewer experimental points per peak); this impacts our estimation

of Q values, particularly again for peaks with lower heights. Furthermore, while our simulations presented below assume the lowest-order radial mode index ($q = 1$), oscillation in higher-order radial modes could also contribute to the range of observed Q values [40].

The uncontrolled nature of the outcoupling of the laser radiation from our micropedestal into free space implies that other microlaser demonstrations, for example, those in the form of periodic arrays on highly reflective substrates, exhibit laser emission exceeding the fluorescence intensity by a greater factor [4,5]. In our results the laser emission peak has a maximum intensity limited to around 1.95 times the broad fluorescence peak, similar to other works including Refs. [18,40–42].

Note that while we have presented results derived from one specific sample, we have fabricated tens of coated microresonators, with a comparable lasing behavior. Our microresonators to date range in height from 40 μm to 200 μm and in radius from 20 μm to 100 μm. The Q values and lasing thresholds are comparable across our set of samples.

The WG mode resonant wavelengths can be obtained from solving the following equation for λ (for particular values of the indices azimuthal m and radial q indices) [30,41]:

$$\frac{1}{\lambda} = \frac{1}{2\pi R n_s(\lambda)} \left(v + 2^{-\frac{1}{3}} \alpha_q v^{\frac{1}{3}} - \frac{P(\lambda)}{(n(\lambda)^2 - 1)^{\frac{1}{2}}} \right.$$
$$\left. + \frac{3}{10} 2^{-\frac{2}{3}} \alpha_q^2 v^{-\frac{1}{3}} - \frac{2^{-\frac{1}{3}} P(\lambda)(n(\lambda)^2 - \frac{2}{3} P(\lambda)^2)}{(n^2(\lambda) - 1)^{\frac{3}{2}}} \alpha_q v^{-\frac{2}{3}} \right),$$
$$\tag{2}$$

where R is the pedestal radius $P(\lambda) = n(\lambda)$ for a TE mode and $P(\lambda) = 1/n(\lambda)$ for a TM mode, with $n(\lambda) \equiv n_s(\lambda)/n_d(\lambda)$, with $n_s(\lambda)$ and $n_d(\lambda)$ the substrate (SU8) and dye (R6G) indices of refraction. In Eq. (2), $v = m + 1/2$ and α_q represents the zeros of the Airy function $\text{Ai}(-z)$. We can obtain the dispersion relation of the WG modes $n_{\text{eff}}(\lambda)$ as $n_{\text{eff}}(\lambda) = m\lambda'/L$, with $L = 2\pi R$, [30,41] and where λ' is the reciprocal of the right-hand side of Eq. (2). Note that the substrate (SU8) index of refraction n_s is obtained from the Cauchy formula $n_s(\lambda) = (A + B/\lambda^2 + C/\lambda^4)$, with $A = 1.566$, $B = 0.00796$, and $C = 0.00014$. Note also that we lack the means to measure the index of refraction for the dye (R6G). Experimentally reported values are within the range 1.35 to 1.55, depending on the concentration [43–45]; in our case, for which R6G is in the form of a thin film, we have assumed a constant value of $n_d(\lambda) = 1.55$.

In Fig. 5 we illustrate the behavior of the WG modes, the associated dispersion relation, and the expected FSR. For this analysis we assume $q = 1$, corresponding to a single radial intensity lobe close to the substrate–dye interface.

Note that for a given radius R, a resonance wavelength λ_m (a tooth of the resulting frequency comb) will correspond to each value of m. These resonance wavelengths λ_m can be obtained by numerically solving Eq. (2). In Fig. 5(a) we show the frequency comb, obtained in this manner, associated with a pedestal for three values of R, e.g., 26 μm, 27 μm, and 28 μm, chosen around the experimental value of $\sim 27 \ \mu$m. In Fig. 5(b) we show the WG mode radial intensity distribution for three distinct
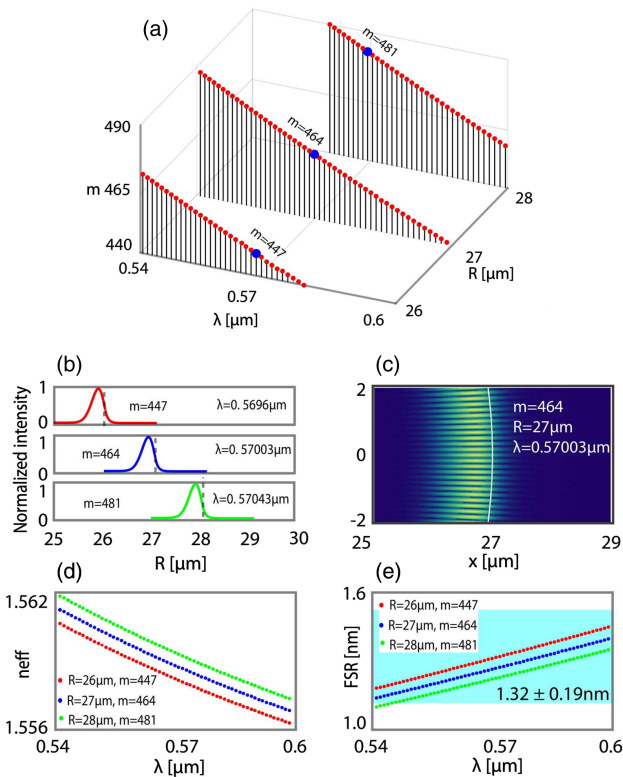
Fig. 5. (a) Resonant wavelengths, as a function of the azimuthal mode index m, in the R6G-coated SU8 micropedestal for three different radii. (b) Radial intensity distributions for three different combinations of R and m. (c) Intensity distribution on $xn - y$ plane for $R = 27$ µm and $m = 464$. (d) Dispersion relation $n_{\text{eff}}(\lambda)$ and (e) free spectral range vs λ for the same three combinations of R and m as in panel (b).

combinations of R and m, indicated with blue dots in panel (a). Note that the evanescent-field intensity extends ~0.4 µm into the dye film and thus ensures that the flux in the WG mode can interact with the dye.

In Fig. 5(c) we show the intensity on the $x-y$ plane, along a section of the pedestal perimeter, for the situation corresponding to the middle plot in panel (b) with $R = 27$ µm. In Fig. 5(d) we show the dispersion relation $n_{\text{eff}}(\lambda)$ for the same three combinations of R and m as in panel (b). In Fig. 5(e) the FSR calculated as FSR $= |\lambda_m - \lambda_{m+1}| \approx \lambda_m^2 / L n_{\text{eff}}$ is presented. We indicate the experimentally obtained range of FSR values, see the histogram in Fig. 4(c), as a horizontal blue-colored band, clearly overlapping with our simulations.

4. CONCLUSION

In summary, we have fabricated organic micropedestals through a low-cost direct laser writing fabrication system built in our laboratory and subsequently coated them with rhodamine 6G dye. The emission characteristics, upon excitation with a laser beam at 532 nm, show that our devices present narrow lasing peaks emerging from the broad fluorescence peak as the pump fluence is increased. The Q values of our lasing peaks are within the range ~450 to ~2300, while the experimentally observed FSR is ~1.3 ± 0.19 nm, coinciding well with our

dispersion simulations based on the WG modes supported by our micropedestal cavities. The observed lasing threshold occurs at a pump fluence of ~5 µJcm^{-2}. We have presented numerical simulations to elucidate the focal shift, which can occur in the printing process for thick layers and a relatively large refractive index contrast at the photoresist top surface. We hope that our work will contribute to further progress in low-cost fabrication of microstructures, particularly microlasers, for a variety of applications.

Disclosures. The authors declare no conflicts of interest.

REFERENCES

1. V. V. Parsi Sreenivas, A. Winkler, S. Harazim, and O. G. Schmidt, "Ultraviolet transmittance of SU-8 photoresist and its importance in multi-wavelength photolithography," J. Vac. Sci. Technol. B **36**, 051601 (2018).
2. J. Lee, K.-H. Choi, and K. Yoo, "Innovative su-8 lithography techniques and their applications," Micromachines **6**, 1–18 (2015).
3. X. Ouyang, Z. Yin, J. Wu, A. P. Zhang, and C. Zhou, "Fabrication of dual-focus microlens array by using dynamic optical projection stereolithography," in Conference on Lasers and Electro-Optics/Pacific Rim, (Optical Society of America, 2018), pp. Th4H-6.
4. V. D. Ta, S. Yang, Y. Wang, Y. Gao, T. He, R. Chen, H. V. Demir, and H. Sun, "Multicolor lasing prints," Appl. Phys. Lett. **107**, 221103 (2015).
5. J. Zhao, Y. Yan, Z. Gao, Y. Du, H. Dong, J. Yao, and Y. S. Zhao, "Full-color laser displays based on organic printed microlaser arrays," Nat. Commun. **10**, 1–7 (2019).
6. M. T. Do, T. T. N. Nguyen, Q. Li, H. Benisty, I. Ledoux-Rak, and N. D. Lai, "Submicrometer 3d structures fabrication enabled by one-photon absorption direct laser writing," Opt. Express **21**, 20964–20973 (2013).
7. D. T. T. Nguyen, Q. C. Tong, I. Ledoux-Rak, and N. D. Lai, "One-step fabrication of submicrostructures by low one-photon absorption direct laser writing technique with local thermal effect," J. Appl. Phys. **119**, 013101 (2016).
8. V. A. Camarena-Chávez, R. Castro-Beltrán, O. M. Medina-Cázares, J. U. Álvarez-Martnez, G. Ramos-Ortz, and G. Gutiérrez-Juárez, "Implementation and assessment of a low-cost 3d laser platform controlled by open software for printing polymeric micro-structures," J. Micromech. Microeng. **30**, 035010 (2020).
9. J. Bigeon, N. Huby, J.-L. Duvail, and B. Bêche, "Injection and waveguiding properties in su8 nanotubes for sub-wavelength regime propagation and nanophotonics integration," Nanoscale **6**, 5309–5314 (2014).
10. N. Tsutsumi, J. Hirota, K. Kinashi, and W. Sakai, "Direct laser writing for micro-optical devices using a negative photoresist," Opt. Express **25**, 31539–31551 (2017).
11. M. T. Do, Q. Li, I. Ledoux-Rak, and N. D. Lai, "Optimization of lopa-based direct laser writing technique for fabrication of submicrometric polymer two-and three-dimensional structures," Proc. SPIE **9127**, 912703 (2014).
12. M. Malinauskas, A. Žukauskas, S. Hasegawa, Y. Hayasaki, V. Mizeikis, R. Buividas, and S. Juodkazis, "Ultrafast laser processing of materials: from science to industry," Light Sci. Appl. **5**, e16133 (2016).

13. J. Schwiedrzik, R. Raghavan, A. Bürki, V. LeNader, U. Wolfram, J. Michler, and P. Zysset, "In situ micropillar compression reveals superior strength and ductility but an absence of damage in lamellar bone," Nat. Mater. **13**, 740–747 (2014).

14. Z. Xiang, H. Wang, A. Pant, G. Pastorin, and C. Lee, "Development of vertical SU-8 microneedles for transdermal drug delivery by double drawing lithography technology," Biomicrofluidics **7**, 066501 (2013).

15. A. Ghanbari, V. Nock, S. Johari, R. Blaikie, X. Chen, and W. Wang, "A micropillar-based on-chip system for continuous force measurement of c. elegans," J. Micromech. Microeng. **22**, 095009 (2012).

16. R. E. Pawinanto, J. Yunas, and A. M. Hashim, "Design optimization of active microfluidic mixer incorporating micropillar on flexible membrane," Microsyst. Technol. **25**, 1203–1209 (2019).

17. B. Zhou, W. Xu, A. A. Syed, Y. Chau, L. Chen, B. Chew, O. Yassine, X. Wu, Y. Gao, and J. Zhang, "Design and fabrication of magnetically functionalized flexible micropillar arrays for rapid and controllable microfluidic mixing," Lab Chip **15**, 2125–2132 (2015).

18. N. B. Tomazio, L. De Boni, and C. R. Mendonca, "Low threshold rhodamine-doped whispering gallery mode microlasers fabricated by direct laser writing," Sci. Rep. **7**, 1–5 (2017).

19. M. Seo, K. Kim, H. Cho, S. Yoon, B. D. Kong, M. Meyyappan, and C.-K. Baek, "Weakly tapered silicon nanopillar resonators with spatially well-separated whispering gallery modes for Si-based lasers," ACS Appl. Nano Mater. **2**, 4852–4858 (2019).

20. M. Lebental, J.-S. Lauret, R. Hierle, and J. Zyss, "Highly directional stadium-shaped polymer microlasers," Appl. Phys. Lett. **88**, 031108 (2006).

21. W. Sun, K. Wang, Z. Gu, S. Xiao, and Q. Song, "Tunable perovskite microdisk lasers," Nanoscale **8**, 8717–8721 (2016).

22. N. Zhang, W. Sun, S. P. Rodrigues, K. Wang, Z. Gu, S. Wang, W. Cai, S. Xiao, and Q. Song, "Highly reproducible organometallic halide perovskite microdevices based on top-down lithography," Adv. Mater. **29**, 1606205 (2017).

23. Y. Li, J. Liu, and S. Sugiyama, "The fabrication and test of a square prism shaped dye micro laser based on the SU-8 molding process," J. Micromech. Microeng. **15**, 1571 (2005).

24. A. H. Fikouras, M. Schubert, M. Karl, J. D. Kumar, S. J. Powis, A. Di Falco, and M. C. Gather, "Non-obstructive intracellular nanolasers," Nat. Commun. **9**, 1–7 (2018).

25. S. Wan, F.-J. Shu, R. Niu, G.-C. Guo, C.-L. Zou, and C.-H. Dong, "Perpendicular coupler for standing wave excitation and wavelength selection in high-Q silicon microresonators," Opt. Express **28**, 15835–15843 (2020).

26. L. E. Helseth, "Focusing of atoms with strongly confined light potentials," Opt. Commun. **212**, 343–352 (2002).

27. J. J. Stamnes, *Waves in focal regions: propagation, diffraction and focusing of light, sound and water waves* (Routledge, 2017).

28. Z.-C. Geng, Z.-F. Zhou, H. Dai, and Q.-A. Huang, "A 2d waveguide method for lithography simulation of thick SU-8 photoresist," Micromachines **11**, 972 (2020).

29. K. J. Vahala, "Optical microcavities," Nature **424**, 839–846 (2003).

30. R. Chen, H. Sun, and T. Van Duong, "Controllable polarization of lasing emission from a polymer microfiber laser," Sci. Rep. **9**, 1–6 (2019).

31. R. Castro-Beltran, N. Huby, G. Loas, H. Lhermite, D. Pluchon, and B. Bêche, "Improvement of efficient coupling and optical resonances by using taper-waveguides coupled to cascade of uv210 polymer micro-resonators," J. Micromech. Microeng. **24**, 125006 (2014).

32. J. Heebner, R. Grover, T. Ibrahim, and T. A. Ibrahim, *Optical Microresonators: Theory, Fabrication, and Applications* (Springer Science & Business Media, 2008), vol. **138**.

33. S.-Y. Lu, H.-H. Fang, J. Feng, H. Xia, T.-Q. Zhang, Q.-D. Chen, and H.-B. Sun, "Highly stable on-chip embedded organic whispering gallery mode lasers," J. Lightwave Technol. **32**, 2415–2419 (2014).

34. Y.-Z. Huang, Q.-F. Yao, X.-M. Lv, J.-L. Xiao, Y. Du, Y.-D. Yang, and J.-D. Lin, "InAlGaAs/InP cylinder microlaser connected with two waveguides," Electron. Lett. **47**, 929–930 (2011).

35. T. Kobayashi and M. Vavasseur, "Single-mode laser emission at 825 nm from a photopumped cylindrical microresonator based on a polymer semiconductor," J. Opt. Soc. Am. B **27**, 2014–2019 (2010).

36. V. Duong Ta, R. Chen, L. Ma, Y. Jun Ying, and H. Dong Sun, "Whispering gallery mode microlasers and refractive index sensing based on single polymer fiber," Laser Photon. Rev. **7**, 133–139 (2013).

37. C. Huang, W. Sun, S. Liu, S. Li, S. Wang, Y. Wang, N. Zhang, H. Fu, S. Xiao, and Q. Song, "Highly controllable lasing actions in lead halide perovskite–Si_3N_4 hybrid micro-resonators," Laser Photon. Rev. **13**, 1800189 (2019).

38. R. Chen, V. D. Ta, and H. Sun, "Bending-Induced bidirectional tuning of whispering gallery mode lasing from flexible polymer fibers," ACS Photon. **1**, 11–16 (2014).

39. S. Gladyshev, A. Bogdanov, P. Kapitanova, M. Rybin, K. Koshelev, Z. Sadrieva, K. Samusev, Y. Kivshar, and M. Limonov, "High-Q states and strong mode coupling in high-index dielectric resonators," J. Phys. Conf. Ser. **1124**, 051058 (2018).

40. F. Tabataba-Vakili, L. Doyennette, C. Brimont, T. Guillet, S. Rennesson, E. Frayssinet, B. Damilano, J.-Y. Duboz, F. Semond, I. Roland, M. El Kurdi, S. Checoury, X. Sauvage, B. Gayral, and P. Boucaud, "Blue microlasers integrated on a photonic platform on silicon," ACS Photon. **5**, 3643–3648 (2018).

41. L. Zhang, Y.-X. Wang, F. Zhang, and R. O. Claus, "Observation of whispering-gallery and directional resonant laser emission in ellipsoidal microcavities," J. Opt. Soc. Am. B **23**, 1793–1800 (2006).

42. Z. Xu, J. Tong, X. Shi, J. Deng, and T. Zhai, "Tailoring whispering gallery lasing and random lasing in a compound cavity," Polymers **12**, 656 (2020).

43. K. Das, S. Mehta, and R. Singh, "Blue shifts and refractive index of rhodamine 6g doped polycarbonate," in *AIP Conference Proceedings*, (AIP, 2011), vol. **1349**, pp. 1317–1318.

44. C. Sánchez-Pérez and A. García-Valenzuela, "Spectroscopic refractometer for transparent and absorbing liquids by reflection of white light near the critical angle," Rev. Sci. Instrum. **83**, 115102 (2012).

45. D. Nilsson, S. Balslev, and A. Kristensen, "Polymer microcavity dye laser based on a single-mode su-8 planar waveguide," Proc. SPIE **5707**, 208–216 (2005).